NANO LETTERS

pubs.acs.org/NanoLett

Controlled Synthesis of Uniform Cobalt Phosphide Hyperbranched Nanocrystals Using Tri-*n*-octylphosphine Oxide as a Phosphorus Source

Haitao Zhang,[†] Don-Hyung Ha,[†] Robert Hovden,[‡] Lena Fitting Kourkoutis,[‡] and Richard D. Robinson*[,†]

[†]Department of Materials Science and Engineering and [‡]School of Applied and Engineering Physics, Cornell University, Ithaca, New York 14853, United States

ABSTRACT A new method to produce hyperbranched Co_2P nanocrystals that are uniform in size, shape, and symmetry was developed. In this reaction tri-*n*-octylphosphine oxide (TOPO) was used as both a solvent and a phosphorus source. The reaction exhibits a novel monomer-saturation-dependent tunability between Co metal nanoparticle (NP) and Co_2P NP products. The morphology of Co_2P can be controlled from sheaflike structures to hexagonal symmetric structures by varying the concentration of the surfactant. This unique product differs significantly from other reported hyperbranched nanocrystals in that the highly anisotropic shapes can be stabilized as the majority shape (>84%). This is the first known use of TOPO as a reagent as well as a coordinating background solvent in NP synthesis.

KEYWORDS Phosphide, TOPO, hyperbranched, crystal splitting, cyclic twinning.

Metal phosphides are an interesting class of materials because their anion electronegativity and interatomic spacing place them between pure metals and metal oxides.[1,2] Bulk transition metal phosphides can display a wide range of properties including superconductivity, catalytic activity, ferromagnetism, magnetoresistance, and magnetocaloric effects and act as semiconductors.[3−6] Cobalt phosphides have been studied because of their interesting magnetic, catalytic, and anode-material properties.[7−12] Common stoichiometries of cobalt phosphides are CoP, Co_2P, CoP_2, and CoP_3.[13−15] Recently, interest in Co_2P has grown since it has been shown to photocatalytically degrade organic dyes and it can act as a catalyst in hydrodesulfurization reactions.[9−11]

Transition metal phosphide nanoparticles are, however, difficult to synthesize because they can adopt a wide range of stoichiometries and because traditional phosphide sources are highly reactive, air sensitive, and toxic.[1,6,16] Therefore, synthesis—including shape and composition control—of nanoscale metal phosphide materials is mostly undeveloped, and it is unclear how their properties are affected at the nanoscale.[1,5] Among *metal phosphides*, InP represents the best studied nanoscale material to date, often using $P[Si(CH_3)_3]_3$ as phosphorus source.[17−21]

Previous work on *nanoparticle* Co_2P have relied upon highly reactive phosphide sources including sodium phosphide,[16] white phosphorus (P_4),[10,22−24] tri-*n*-octylphosphine (TOP),[25] and triphenylphosphine (PPh_3).[26] Sodium phosphide and white phosphorus have been predominately used in solvothermal methods, which invariably leads to aggregated particles with no size or shape control, and with mixed CoP and Co_2P compositions.[6,16,22] For the TOP reactions a Co−TOP complex was slowly added to a heated, air-free flask of tri-*n*-octylphosphine oxide (TOPO), producing rodlike Co_2P.[25] PPh_3 was used as a phosphorus source in an Ullmann-type reaction and aggregated Co_2P nanowires were synthesized.[26] These reactions often resulted in a mixture of products, and an extra purification process was required to get pure Co_2P. Recently a single source precursor method has been reported to produce CoP and Co_2P nanoparticles.[27] While this work is encouraging, the particles lack shape control and are not monodisperse and X-ray diffraction (XRD) indicates a pure phase of Co_2P was not obtainable.

Kinetic control of nanoparticle growth gives the possibility for greater control of anisotropic growth shapes, such as rods, tetrapods, arrow shapes, sheaflike shapes, branched crystals, and hyperbranched structures.[28−32] Anisotropic nanocrystals could serve as a test bed for growth theories. Despite decades of study, a quantitative understanding of crystallization is generally unknown and the formation of nonequilibrium crystal shapes in nature is not understood.[33,34] Holistic treatments of the processes necessary to produce the many complexly shaped nanocrystals are in their infancy.[35]

In this paper we present the first use of TOPO, an air-stable compound, as a controlled phosphorus source for the

* To whom correspondence should be addressed, rdr82@cornell.edu.
Received for review: 9/27/2010
Published on Web: 12/09/2010

DOI: 10.1021/nl103400a | *Nano Lett.* **2011,** *11,* 188–197

TABLE 1. Summary of the Reactions of Precursors I−VI in TOPO at 350 °C

	$Co(OA)_2$					
	precursor **I**	precursor **II**	precursor **III**	$Co(acac)_2$ precursor **IV**	$Co(OA)_{1.5}(acac)_{0.5}$ precursor **V**	$Co(OA)_{1.8}(acac)_{0.2}$ precursor **VI**
Co:L[a]	1: 2.2	1: 3	1: 5		1: 1.5	1: 1.8
time (min)[b]	6	10	60	6	6	6
product	Co_2P (**1**)	Co_2P (**2**)	Co_2P (**3**)	Co (**7**)	Co_2P + Co (**8**)	Co_2P (**9**)

[a] Molar ratios. L is the sum of oleate ligand and oleic acid. [b] The reaction time was accounted from precursor injection to removal of heating mantle. The reaction flask was then allowed to slowly cool down in air.

synthesis of hyperbranched Co_2P. The hyperbranched particles are unique in that the majority of the product (>84%) possesses the same symmetry, size, and structure, which to date has not been the case for hyperbranched transition metal phosphides and most other hyperbranched nanoparticle systems. We report on the first wide-scale growth of cyclic twin nuclei that lead to star-shaped Co_2P nanocrystals, and we also discuss a novel mechanism that allows for control of the chemical composition of nanocrystal products based solely on the saturation of monomers.

Co_2P nanocrystals were synthesized by decomposing $Co(OA)_2$ in TOPO at 350 °C. The $Co(OA)_2$ complexes were prepared by the ligand exchange reaction between $Co(acac)_2$ (acac = acetylacetonate) and oleic acid (HOA, OA = oleate; see Supporting Information for detailed synthesis and characterization). Co_2P nanoparticles (NPs) were then produced by injecting the precursor into a hot (350 °C) flask of TOPO under air-free conditions. The reaction was stopped by simple removal of the heating mantle after the nanoparticles completed their growth (by examining aliquots). We have confirmed that TOPO was the only phosphorus source in the synthesis and thus acted not only as a solvent but also as a reaction reagent providing phosphorus for the formation of Co_2P NPs (see Supporting Information).

The amount of free oleic acid in the precursor has a significant influence on the sizes and morphologies of the products. The reactions of $Co(OA)_2$ precursors with different amounts of oleic acid are summarized in Table 1. Hyperbranched "sheaflike" Co_2P nanocrystals (**1**) (Figure 1a) were obtained from the reaction of precursor **I**. The product **1** resembles the structures reported recently in the Bi_2S_3[32] and Fe_2P[5] systems, but the entire yield of NPs reported here is uniform in shape and size (half-sheaf length 81 ± 4 nm, 5% standard deviation), unlike those reported in the Bi_2S_3 and Fe_2P systems. Upon increase of the oleic acid concentration (precursors **II** and **III**), the reaction was significantly slowed down (Table 1), resulting in larger size hyperbranched Co_2P nanoparticles (**2** and **3**, Figure 1c,e) with different morphologies.

Electron and X-ray powder diffraction (XRD) confirmed that the phase of **1**−**3** is Co_2P. All the peaks in the XRD spectra of **1**−**3** can be indexed to orthorhombic Co_2P (PDF 89-3030) with no indication of other crystal phases (Figure 1b). The selected area electron diffraction (SAED) patterns (Figure 1d and Figure S3 in the Supporting Information) taken on **2** and **3** are consistent with the (112), (211), (020), (302), (123), (321), and (322) planes of the orthorhombic Co_2P structure. High-resolution transmission electron microscopy (HR-TEM) images of **1** and **3** (Figure S4a in the Supporting Information and Figure 1f) revealed that the nanofilaments grow along the [020] direction. The growth direction was also supported by the relative peak intensity of (020) compared to the other peaks in the XRD patterns of products **1**−**3** (Figure 1b). An amorphous layer was observed in HR-TEM (Figure 1f), which might be formed during synthesis or from the decomposition of crystalline Co_2P phase under the high energy electron beam. Single-nanoparticle SAED (Figure 2) indicated that the filaments in each arm of **3** aligned along the common axis with the same preferred orientation. Streaks in the SAED patterns of Figure 2 are caused by small angle deviations of filaments in each bundle arm.

The major component of **1** is two-arm bundles (84%, Figure S5a in the Supporting Information), while the three- and four-arm structures significantly increase in **2** (Figure S5b in the Supporting Information), and the six- and five-arms dominate the morphology of **3** (Figure S5c in the Supporting Information). Although three- and four-arm particles are also observed in **3**, it is worth noting that all nearest neighbor arms are spaced at multiples of 60° regardless of the number of arms in the NPs (Figure S6 in the Supporting Information). The individual nanofilaments that make up the large arms have an average diameter of ∼4 nm in **1** and **2**, while this number increases to ∼7 nm in **3**. The length of the arms also increases from **1** (81 ± 4 nm) through **2** (122 ± 8 nm) to **3** (360 ± 30 nm). Thus the maximum dispersity in this dimension is always better than 10% for nanocrystals **1**−**3**. Such size and morphology controllability has not been observed in the previously reported hyperbranched structures.

Panels a−c of Figure 3 show scanning electron microscopy (SEM) images of **3**. Each arm of **3** is three-dimensional, but for most of the particles the different arms are approximately in the same plane as seen by SEM (Figure 3a,b) and electron tomography (Figure 3d−g, movie 1). Only ca. 3% of the particles exhibit a three-dimensional arm arrangement (Figure 3c). It is interesting that with the increase in sizes, the shapes of the arms change from sheaflike (**1**) to conelike (**3**).

TOPO is generally considered to be a very stable tertiary phosphine oxide[36] and only acted as an innocent solvent or weakly coordinating surfactant ligand in the synthesis of colloidal nanocrystals. To further understand the formation mechanism of Co_2P with TOPO as a phosphorus source, we

DOI: 10.1021/nl103400a | *Nano Lett.* **2011,** *11,* 188−197

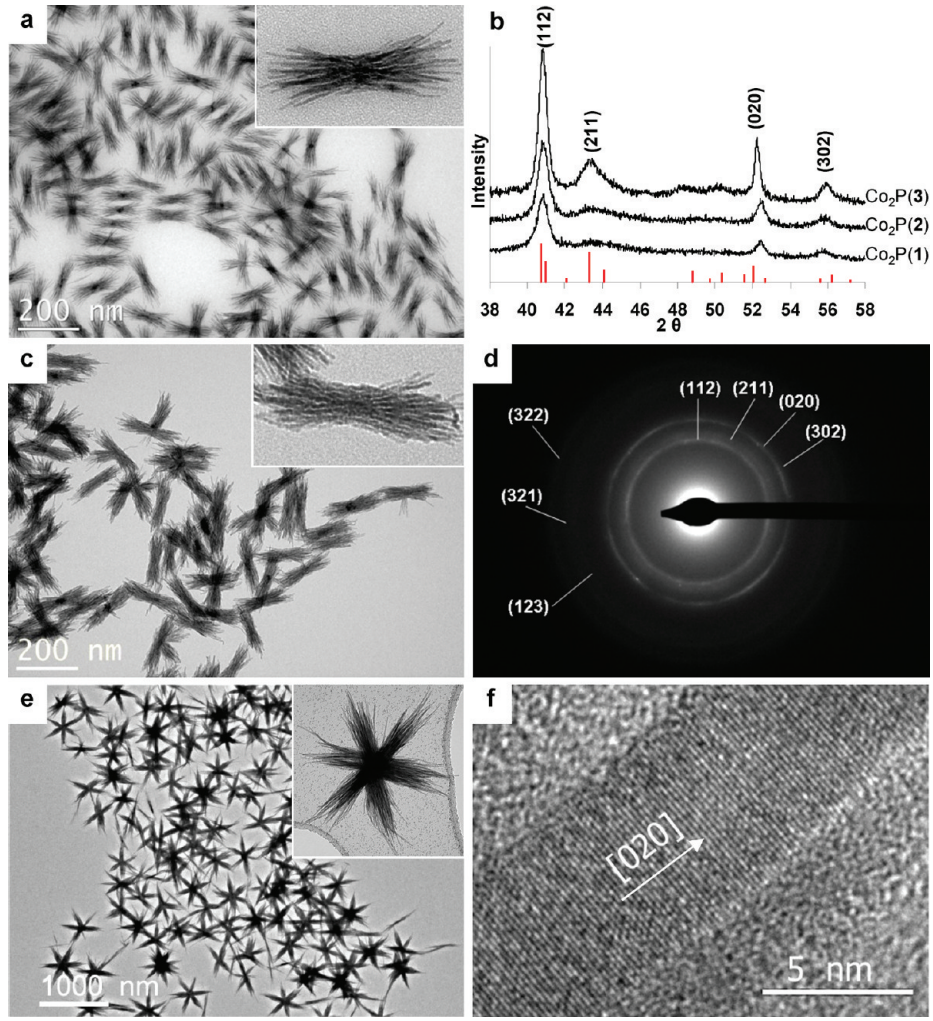

FIGURE 1. TEM images of Co_2P products 1 (a), 2 (c), and 3 (e). Powder XRD patterns of products 1, 2,, and 3 (b), and the red stick pattern corresponds to PDF 89-3030 (Co_2P). SAED pattern of 2 (d). HR-TEM image of nanocrystal 3 (f).

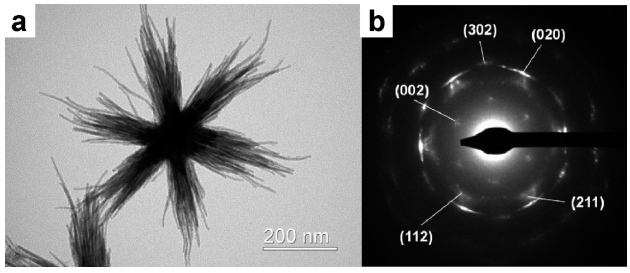

FIGURE 2. TEM image of nanoparticle 3 (a) and the corresponding single nanocrystal SAED pattern (b). The diffraction pattern is indexed to the Co_2P orthorhombic crystal unit cell (PDF 89-3030). Image (a) is a representation of nanoparticle 3 from single nanocrystal SAED.

undertook a series of studies on the reaction conditions, such as temperature, precursor ligands, and precursor concentrations. We found that all these factors have significant influence on the reactions, and the nanocrystal products can be tuned from Co_2P to Co metal by simply varying these synthetic parameters. We propose that the Co monomer (atom or subnanometric cluster) is a reactive intermediate in these reactions as its concentration was found to be crucial in controlling the chemical composition of the final nanocrystal product.

We examined the reactions of precursor **I** at different temperatures (Table 2). It was found that keeping a high temperature (>340 °C) is crucial to obtain a pure Co_2P product. When the reaction of precursor **I** was carried out at 330 °C, a mixture of Co_2P and hexagonal close packed (hcp) Co metal NPs (**4**) was produced (Figure S7 in the Supporting Information). When the reaction of precursor **I** was kept at 350 °C for 3 min and then slowly cooled down, a novel Co−Co_2P heterostructure (**5**) (Figure S8 in the Supporting Information) was obtained. The heterostructure **5** is composed of a hcp Co metal core (polycrystalline, ca. 30 nm in diameter) as determined from the lattice spacing measured using HR-TEM (Figure S8c in the Supporting Information) with Co_2P filaments radiating from this core (the filaments were identified as Co_2P based on the XRD pattern). It is interesting to note that the Co metal forms predominately at the core of the particles in **5**. In comparison

DOI: 10.1021/nl103400a | *Nano Lett.* **2011,** *11,* 188–197

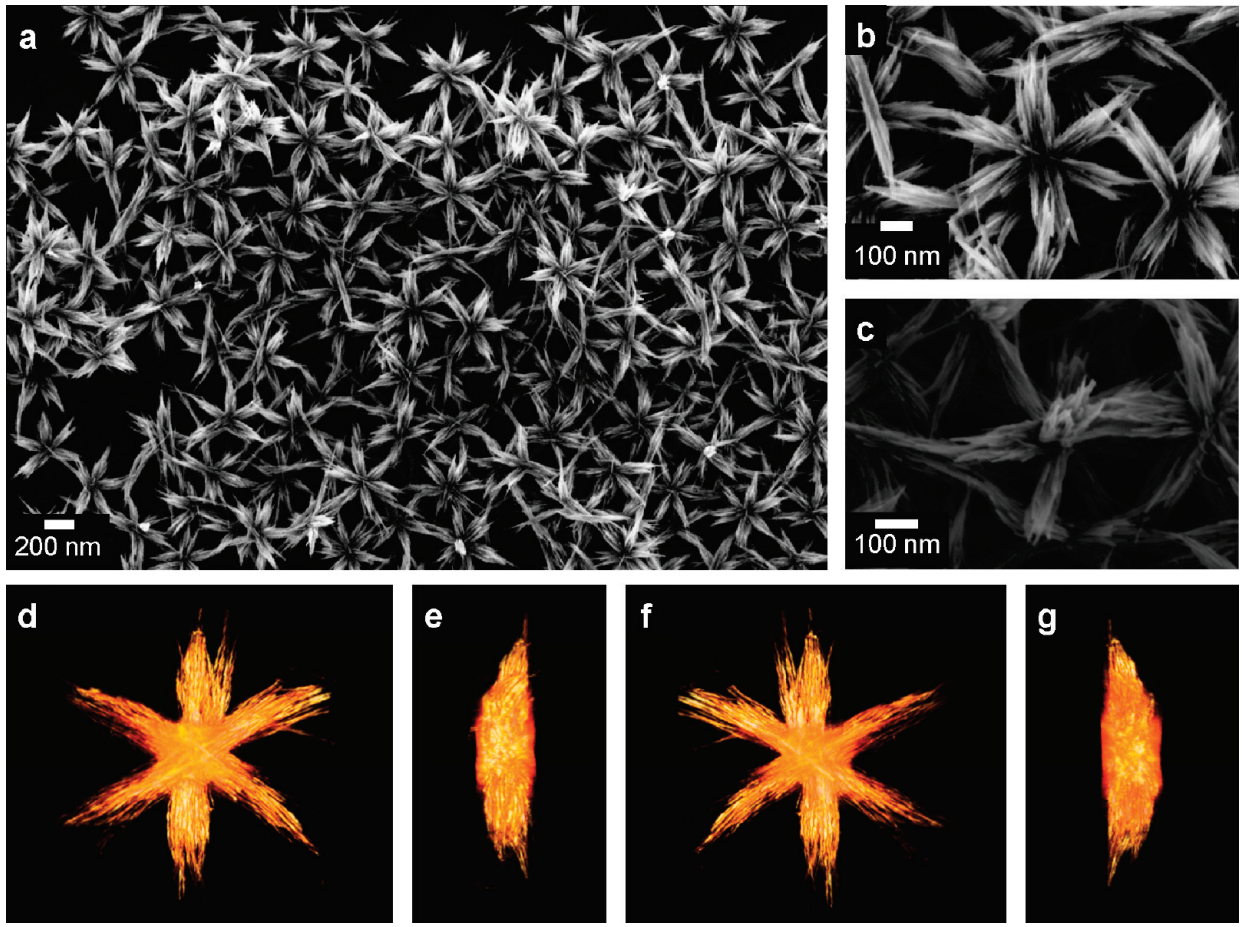

FIGURE 3. SEM images (a−c) and electron tomography reconstruction (d−g) of Co_2P (3). The majority of structures are planar (a, b, d−g), while a few show three-dimensional growth (c). Images d−g show a single structure rotated 360° about a vertical axis visualized by direct volume rendering of the tomographic reconstruction. Rough segmentation was performed to reduce artifacts and to remove fiduciary gold particles for clarity. The "front" perspective (d) has the flat side at the back of the image while the "back" (f) has the flat side at the top of the image. Images e and g show the right and left perspective of the particle. The flat side occurs where the particle is in contact with the TEM grid and is likely due to capillary forces during drying.

TABLE 2. Summary of the Reactions of Precursor I in TOPO

temperature (°C)	350[a]	330[a]	350[a]	350[b]
time (min)	6	6	3	3
product	Co_2P (**1**)	Co + Co_2P (**4**)	Co − Co_2P heterostructure (**5**)	Co_2P (**6**)

[a] The reaction was stopped by simple removal of the heating mantle, and the reaction flask was allowed to slowly cool down in air. [b] The reaction was stopped by injecting the reaction solution into cold ethanol.

to this previous reaction, when the reaction of precursor **I** was kept at 350 °C for 3 min and then an aliquot was taken and immediately quenched (injection into cold ethanol), only small Co_2P hyperbranched bundles (**6**, Figure 4c) formed (no Co metal was detected by XRD). This proves that the Co metal in the heterostructure **5** is coming from the decomposition of the unreacted precursor **I** at lower temperatures during the cooling process. These observations indicate a possible formation method of Co_2P in our synthesis, that is, decomposition of cobalt oleate produces Co, which reacts with TOPO at a high temperature (350 °C) and generates Co_2P.

We found that the ligand of the Co precursor played an important role in the reaction. When $Co(acac)_2$ (precursor **IV**) was used as the precursor with the other reaction conditions, the same as in the synthesis of compound **1** (350 °C, 6 min, 0.15 mmol Co/5 g TOPO), hcp Co nanoparticles (**7**) were isolated as the only product (Figure S9a,d in the Supporting Information and Table 1). The decomposition of $Co(acac)_2$ appeared to be much faster than that of $Co(OA)_2$ precursors, and the reaction solution turned dark immediately upon the injection of the precursor. When the reaction of $Co(acac)_2$ in TOPO was kept for 5 h at 350 °C, most of the Co metal was found to be transformed into Co_2P, as detected by the powder XRD analysis (Figure S10 in the Supporting Information). This result proves that the Co metal formed during the reaction can be converted into Co_2P by the further reaction with TOPO. Such two-step reactions have been observed before in the synthesis of metal phosphides by using tri-*n*-octylphosphine (TOP) as a phosphorus source.[37−40] A catalytic decomposition of TOP induced by metal was proposed as the mechanism for these reactions.

DOI: 10.1021/nl103400a | *Nano Lett.* **2011,** *11,* 188−197

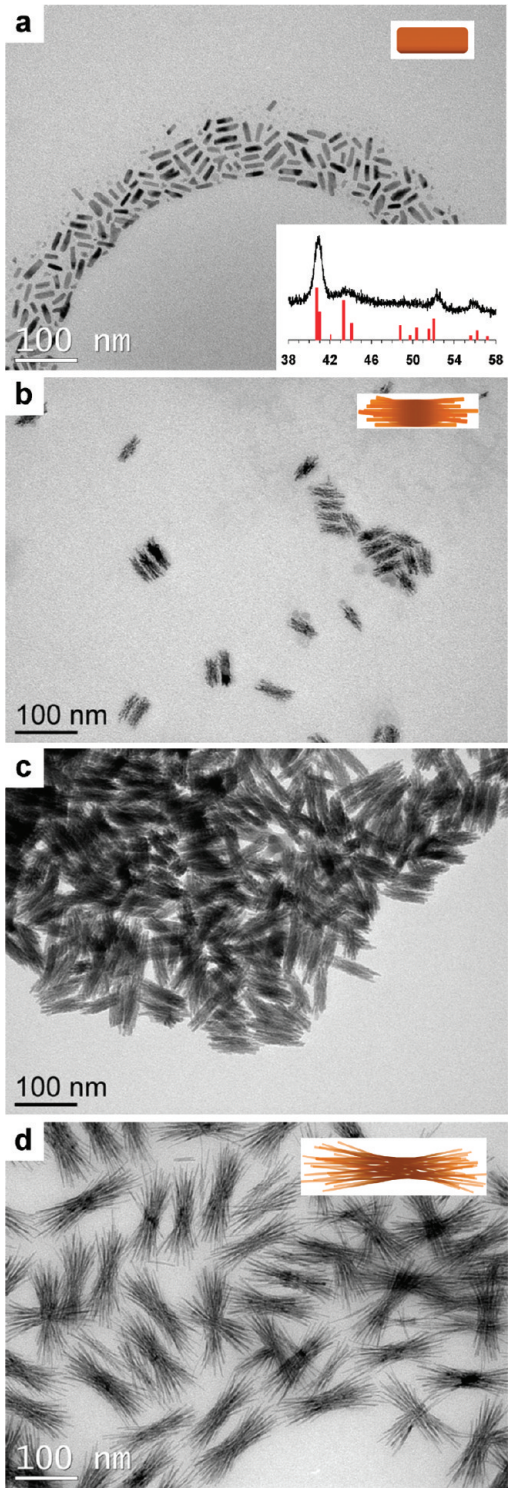

FIGURE 4. TEM images of the morphology evolution of nanocrystal 1: 20 (a), 60 (b), 180 (c), and 360 s (d). The XRD pattern of the 20s nanorods is shown in the inset of (a), and the red stick pattern corresponds to Co_2P (PDF 89-3030).

The reduction/decomposition of tertiary phosphine oxide in the presence of elemental metal at elevated temperature (>300 °C) has been reported in literature,[41] which provides additional support of our proposed reaction mechanism.

SCHEME 1

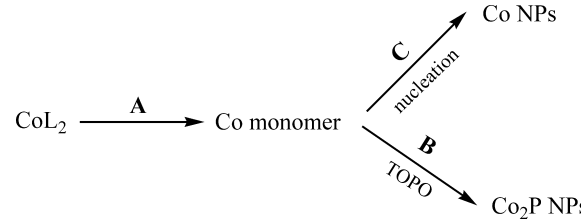

However, this reaction of Co metal NPs with TOPO (Figure S10 in the Supporting Information) needed a much longer time (>5 h) for the complete phase transformation into Co_2P than the synthesis of products **1**−**3** and resulted in NPs of different shapes. Moreover, when aliquots were taken from the reaction of precursor **I** toward generating product **1**, no Co NPs were generated even at the very early stages (Figure 4a). On the basis of these ligand effects studies, the reactions that generated products **1**−**3** produced Co_2P before the formation of Co NPs. In this case, Co monomers (atoms or subnanometric clusters, which are known as extremely reactive species[42]) likely reacted with the TOPO before they were able to form Co NPs (Scheme 1, steps A and B).

Co metal monomers are generated by the reduction and decomposition of CoL_2 (L = OA or acac) precursors at high temperature. Co^{2+} in CoL_2 is reduced to Co metal in the absence of any obvious reductant. The most probable reducing reagent should be the leaving L^- ($acac^-$ or OA^-) ligands (or their decomposition). Moreover, TOPO is known to be capable of promoting the similar reduction reaction in metal complexes.[43] If the concentration of Co monomers is high enough, collisions between Co metal monomers will lead to metal nuclei, which eventually grow to cobalt metal nanoparticles (Scheme 1, path C; the Co metal NPs can be isolated as products because of their low reactivity with TOPO). If, however, the concentration of Co monomers is too low to support nuclei formation, then secondary reactions of the Co monomer with TOPO can occur to produce Co_2P (Scheme 1, path B). Thus, the formation of Co or Co_2P NPs in these reactions mainly depends on the competition of paths B and C, which ultimately is mediated by the concentration of Co monomers. In the reactions of precursors **I**−**III** at 350 °C, path A is slow enough compared to step B that the Co monomer is never supersaturated enough to generate Co NPs. Co_2P nanocrystals were thus produced as the only product (**1**, **2**, **3**). When step A becomes much faster by using a more reactive precursor $Co(acac)_2$ (**IV**), or if step B is halted by lowering the temperature (step A will still continue at lower temperatures since it has a lower activation barrier), the concentration of Co monomers will reach supersaturation and Co NPs will be produced. These processes were observed in the synthesis of nanocrystals **4**, **5**, and **7**, and also substantiated by introducing a higher concentration of *precursor*: when 0.45 mmol of precursor **I** (3 times that of the amount used in the synthesis of Co_2P(**1**)) reacted with 5 g of TOPO at 350 °C, Co metal NPs were obtained as the

DOI: 10.1021/nl103400a | *Nano Lett.* **2011,** *11,* 188–197

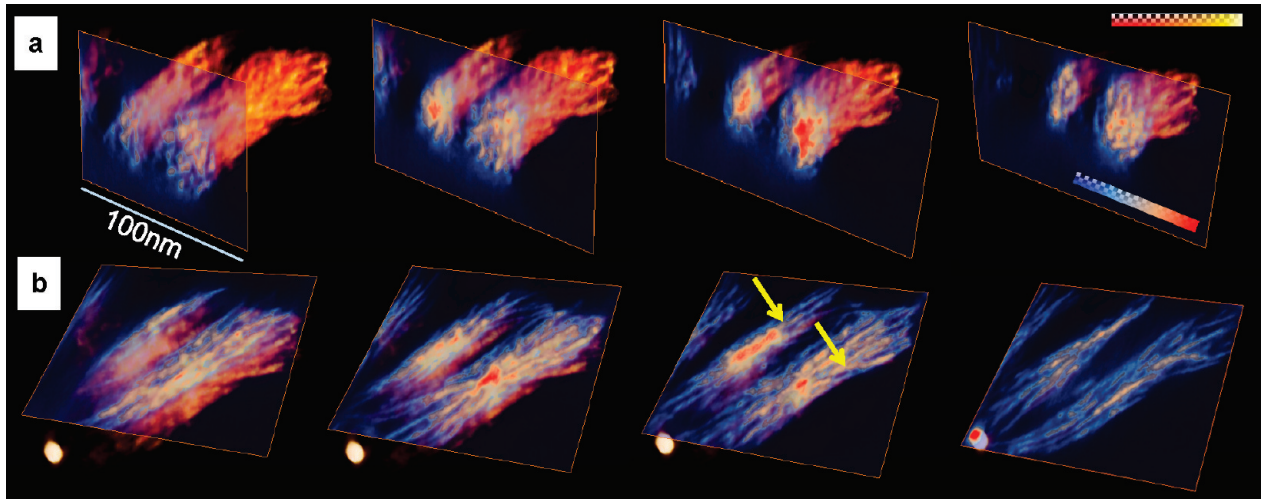

FIGURE 5. Tomographic reconstruction of nanocrystal 1. The three-dimensional structure is shown by direct volume rendering of the reconstruction using a red−yellow−white color scale (top right inset in a). 2D slices from the tomographic reconstruction perpendicular (a) and parallel (b) to the long axis of the hyperbranched structures are displayed using a blue−white−red color scale as shown in the last slice of (a). Yellow arrows in (b) mark the locations of splitting. High intensity at the center of the two individual hyperbranched structures indicates the presence of a solid core in each particle.

major product (Figure S11 in the Supporting Information). Thus, under the same reaction conditions, a greater molar volume of precursor will lead to a higher concentration of Co metal monomers, which then facilitates the nucleation of Co metal NPs. This result provides further support of our general reaction mechanism: the pathways between Co metal NPs and Co_2P NPs are mediated by the concentration of Co monomers.

To further elucidate such phase control, we examined the reactions of precursors $Co(OA)_n(acac)_{2-n}$ with a mixture of ligands ($n = 1.5$ (**V**), 1.8 (**VI**); see Supporting Information for detailed synthesis and characterization). Using the same conditions as in the synthesis of product Co_2P (**1**) (350 °C, 6 min, 0.15 mmol of Co/5 g of TOPO), a mixture of Co metal with a small amount of Co_2P NPs (**8**) was obtained from the reaction of precursor **V** (Figure S9b,e in the Supporting Information), while precursor **VI** produced Co_2P nanoparticles (**9**) as the major product (Figure S9c,f in the Supporting Information). Thus, under the same reaction conditions, with a decrease in the amount of oleate ligands in the precursors, the phases of the NPs products were changed from Co_2P (precursors **I**, **VI**) to a Co_2P and Co metal mixture (precursor **V**) to Co metal (precursor **IV**) (Table 1). Such phase controllability can be directly related to the reactivity of precursors **I** and **IV**−**VI**: less oleate ligand resulted in faster decomposition (based on the color change of the reaction solution), indicating that the oleate ligands provide stronger passivation to the cobalt cations than the acac ligands to stabilize the precursors. These results follow directly from our proposed reaction mechanism and represent an interesting example that not only the size and shape but also the chemical composition of the NPs products can be tuned by the coordination chemistry of the precursor ligands.

We believe two well-known crystal growth phenomena make up the complex structures seen in our Co_2P hyperbranched crystals: crystal splitting and cyclic twinning. Neither mechanism is well understood. In the sheaf structures of Co_2P **1** and **2**, crystal splitting is responsible for creating the nanofilaments that resemble frayed ends. In the star-shaped Co_2P **3**, crystal splitting is responsible for the nanofilament arms and cyclic twinning is responsible for the hexagonally symmetric core.

Crystal splitting describes the branched and split structures that form on a growth front. It is generally associated with fast crystal growth.[31] We studied the morphology evolution of hyperbranched Co_2P nanocrystals by analyzing TEM images of aliquots obtained at different time intervals during a reaction. Figure 4 shows the evolution of nanocrystal **1**. Nanorods were obtained at the very early stage (Figure 4a). Powder XRD (inset of Figure 4a) and HR-TEM (Figure S4b in the Supporting Information) studies have confirmed that the nanorods are Co_2P single crystals. The nanorods grow along the [020] direction, which is the same growth direction as that of the nanofilaments that make up the branches in the sheaf structures **1** (Figure S4a in the Supporting Information) and the major arms of the star structures **3** (Figure 1f). As the reaction proceeds, the nanorods start to split into small nanofilaments along the growth direction. The individual nanofilaments continue to grow, mainly in the elongated direction and finally form the hyperbranched sheaflike structures (Figure 4d). Electron tomography studies show a high density region inside the sheaflike structure **1** and indicate the presence of a solid core (Figure 5),[44] which further suggests that the hyperbranched structure **1** is not aggregates of many individual nanowires but a single crystal growing from the original nanorod with

DOI: 10.1021/nl103400a | *Nano Lett.* **2011,** *11,* 188–197

nanowires splitting at its ends. This process resembles the evolution of hyperbranched Bi_2S_3,[32] but the Bi_2S_3 starts from a more complex shape and no simple unsplit single-crystal stage was initially observed.

The exact cause of crystal splitting is generally unknown and varies depending on the system. The crystal structure of Co_2P (Figure S12 in the Supporting Information)[45] does not possess any one or two-dimensional structural character in the growth direction that would provide the splitting vectors. The asymmetry of its space group *Pnma*, however, can promote fast growth along the *b* axis.[26,46] Electron tomography revealed many kinks in the individual nanowires that make up the arms (Figure 5b), indicating the presence of a high density of crystal defects, and most of the nanowire splitting is found to occur around the kink sites, as shown by the 2D slices through the tomographic reconstruction (Figure 5b).

The crystal splitting appears to occur in an isolated period of time for products **1**, **2**, and **3**. The nanofilaments are all roughly of the same diameter for each product, indicating that splitting/branching occurs early in the growth stages and then greatly diminishes afterward. This is unlike other sheaflike structures, which not only exhibit splitting from the core (as is the majority case in our results) but also show pronounced branching in each filament during the growth.[47]

The progression of the reaction from product **1** to **3** is characterized by (a) longer times (6 min for **1** compared to 1 h for **3**) and (b) thicker nanofilaments (4 nm for **1** compared to 7 nm for **3**). The faster growth in **1** suggests a higher degree of monomer supersaturation than in the reaction of **3** (or a lower barrier for growth, as would be the case if the number of coordinating ligands was lower). These results are consistent with branched solidification patterns, such as spherulites, for which a higher degree of supersaturation results in finer arm features.[48,49] The sheaf structure in our products **1** and **2** clearly resemble the early stage of spherulites (category 2 in Figure 2 of ref 48). Product **3** can also be thought of as a sheaflike structure, albeit with a hexagonal center and thus producing six arms that each have crystal splitting instead of two arms.

When phase field theories are used to model spherulite crystals, the dendritic 3D growth is found to originate from large differences between the rotational and translational diffusion coefficients of molecules.[50,51] A decrease in the rotational/translational ratio implies that the reorientation of molecules attaching to the surface is slow compared to the interface growth propagation and will lead to crystal splitting.[48,50] This ratio decreases for supercooled liquids, leading to a higher degree of branching. The cause is that the greater supersaturation from the supercooled liquid results in faster growth fronts which decrease the distance that solute is rejected by the growth front. The narrow boundary layer then leads to instabilities that ultimately promote branching.[48] One means to test this effect in our system is by adjusting the concentration of the precursor. Although the higher concentration of precursor **I** results in the formation of Co metal NPs as we have described, the slower decomposition of precursor **III** allows us to still get pure Co_2P nanocrystals with increased precursor concentration. When we doubled the concentration of precursor **III** for the synthesis of **3**, the branching greatly increased and closely resembled the final spherulite structure (see Figure S13 in the Supporting Information and compare to Figure 4i in ref 32 and Figure 8c in ref 5), which follows directly from this theory. This suggests a crystal-splitting mechanism similar to that in the spherulites is at work in our system.

The multiarmed structures were obtained as major products in **3** (>98%) and were seen in Bi_2S_3[32] and Fe_2P[5] systems as minor products. Whitmire et al.[5] proposed that such complex symmetric structures formed as a result of a twinning mechanism. A twin is a symmetric intergrowth of two or more crystals of the same substance and results in equal size of different crystals. The six-arm structure in **3** exhibits a highly symmetric structure: arm lengths are all nearly equal (less than 10% diversity in length) and angles between major arms are all roughly 60° (Figure S6d in the Supporting Information). The three-, four-, and five-armed structures of **3** displayed approximately the same arm length and angle spacing as the six-arm particles and only differed by the absence of three, two, or one arm, respectively (Figure S6a–c in the Supporting Information). In other words, a 60° or multiple of 60° (120° or 180°) angular spacing between major arms is retained even in the three-, four-, and five-armed structures indicating a common 6-fold symmetry. Such hexagonal shapes are typical for cyclic twins found in orthorhombic unit cells and have been observed in various minerals.[52] From the dark field (DF) TEM images (Figure 6), it is evident that each opposing arm in the particles of **3** grows with the same orientation (the weak contrast on the core part of **3** might be due to its thickness). The DF TEM studies indicate that a single seed nucleates each crystal and then cyclic twinning occurs in the early stages of growth after nucleation but before the crystal splitting. An aliquot study reveals the formation of multirod particles at the very beginning of the reaction (120 s, Figure 7a), and most of neighbor rods are spaced at approximately multiples of 60°, which is characteristic of the hexagonal cyclic twins found in aragonite and chrysoberyl crystals (Figure 7d).[53] The rods that form the arms in the twin crystal begin to split as shown in the 900 s aliquots (Figure 7b), and the nanofilaments continued to grow along the directions of the rods, finally forming the hyperbranched structures (Figure 7c). It is interesting that all seeds exhibit the cyclic twins. Of the nanocrystals **3**, only 1.6% did not exhibit 6-fold symmetry, while the overwhelming majority of the seeds undergo this identical twinning.

The thickness on the core part of nanoparticles **3** impeded further structural analysis by HR-TEM. In order to obtain structural information from the core region, scanning trans-

DOI: 10.1021/nl103400a | *Nano Lett.* **2011,** *11,* 188–197

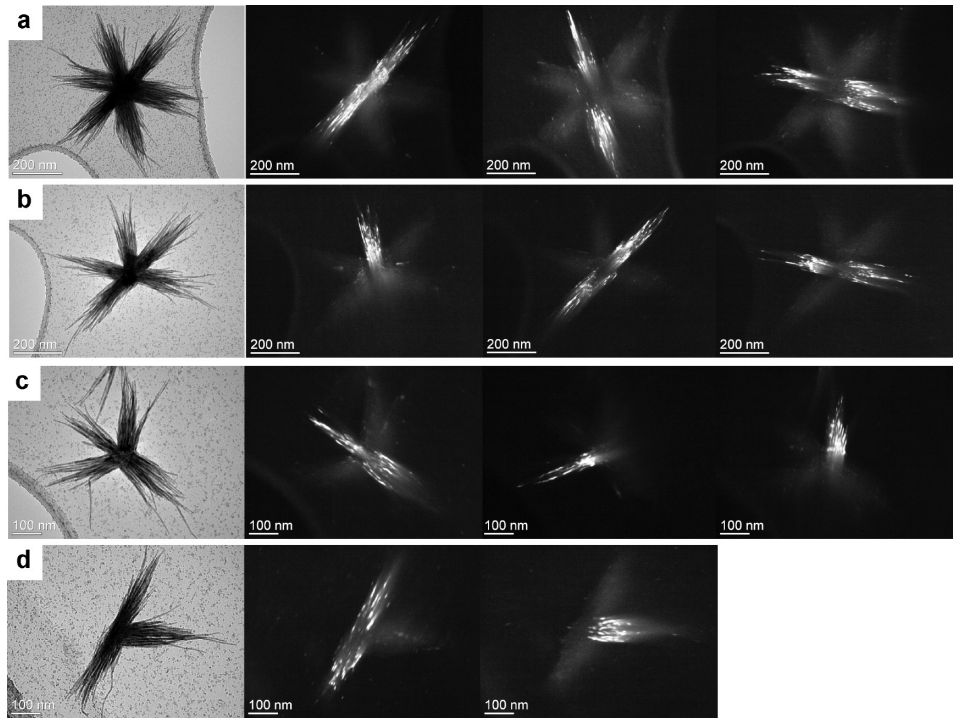

FIGURE 6. Bright and dark field TEM images of the multiple-arm particles in 3, showing crystallographic alignment of opposing arms. This confirms the presence of orthorhombic cyclic twinning which forms hexagonal crystals. The dark field images were obtained by selecting individual (020) diffraction spots.

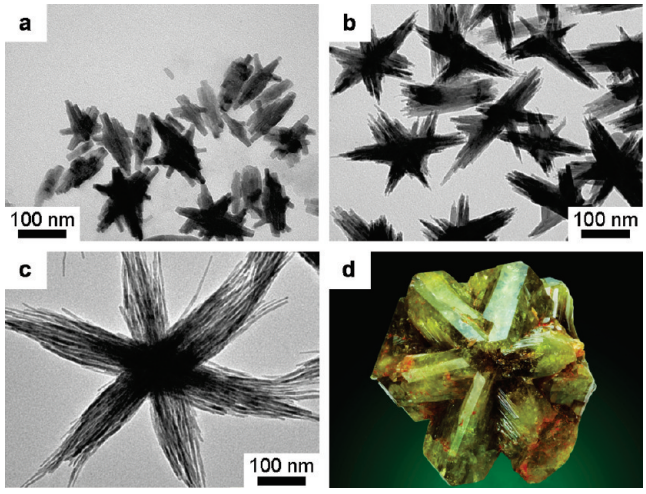

FIGURE 7. TEM images of the morphology evolution of nanocrystal 3: 120 (a), 900 (b), and 3600 s (c). Photograph of cyclic-twinned orthorhombic chrysoberyl ($BeAl_2O_4$) crystal (d, adapted from ref 53).

mission electron microscopy (STEM) tomography was performed. 2D slices from the tomographic reconstruction of nanoparticles **3** revealed a high density at the center of the particle (Figure S14a and movies 2 and 3 in the Supporting Information) and thus indicated the presence of a solid core, which is consistent with the observation that the hyperbranched structures were developed from unsplit particles (Figure 7). It is also interesting to note that the solid core is not always evenly distributed in six arms but often exists in two opposing arms, which is consistent with the nonsymmetric shapes of the early formed particles (Figure 7a).

The formation mechanism of the twin crystals in our product cannot be coalescence as recently proposed for metal twinned particles,[54] because the opposing arms all have identical crystal orientation as shown by DF TEM (Figure 6). Additionally, due to the uniformity of the final product (>98% possess hexagonal symmetry), the nucleation of twins must occur at the same time. Both these data and the growth morphology shown in the aliquots (Figure 7) suggest that cyclic twining is responsible for the hexagonal symmetry in product **3**.

Twinned nanoparticles have appeared in previous literature.[55,56] Most reports for twinned particles involve metals (e.g., Ag, Pt, etc.) and the polyol synthesis method. While great progress has been made in stabilizing twinned crystal nuclei in metals under polyol synthesis, to our knowledge, we are the first to report such a high percentage of cyclic twinned nanoparticles produced through nonaqueous thermal decomposition of metal complex precursors.

The formation of twinning crystals was not observed during the structural evolution of sheaf nanocrystal **1**. The synthesis of **1** and **3** differed by the concentration of oleic acid. Thus the higher concentration of oleic acid used in the synthesis of **3** is a major cause of twinning at the beginning of the crystal growth. Such ligand-induced twinning was also observed for the multiple wurtzite twinning of CdTe,[57] in which more tetrapod twin crystals were obtained by using

DOI: 10.1021/nl103400a | *Nano Lett.* **2011,** *11,* 188–197

a higher concentration of methylphosphonic acid (MPA). It was proposed that the MPA may promote the formation of a twin boundary.[57] It cannot be excluded that oleic acid has a similar templating effect in our synthesis. On the other hand, we found that the Co_2P nanoparticles can be easily dissolved in neat oleic acid at high temperatures (Figure S15a,b in the Supporting Information). The dissolution of Co_2P by the excess oleic acid in the reaction should be a reverse process of the crystal growth (Figure S15c in the Supporting Information). So by increasing the concentration of oleic acid, the nanocrystals with high surface to volume ratios will be less stable, while the formation of twinning crystals, which can decrease the surface area, will be favored.

In conclusion, we report the synthesis of novel Co_2P hyperbranched nanostructures via a simple colloidal solution method. For the first time, we have found that TOPO acted not only as an innocent coordinating solvent but also as a reactive reagent in the synthesis of nanocrystals. The reaction mechanism studies show that TOPO could be a generally useful phosphorus source for the synthesis of metal phosphides. Empirical evidence of the reaction mechanism suggests that the degree of the saturation of Co monomers efficiently tunes the reaction products between Co metal NPs and Co_2P NPs. Such chemical composition control solely by monomer concentration is rare. By variation of the synthetic parameters, the sizes and morphologies of the hyperbranched Co_2P can be controlled from sheaflike structures to six-arm symmetric star structures. The hyperbranched structures likely form by crystal splitting and cyclic twinning. The cyclic twinning mechanism is believed to be responsible for the hexagonal symmetry in star particles.

Acknowledgment. We thank John Grazul, Yuanming Zhang, and Mahmut Aksit for assistance with HRTEM, electron diffraction, and SEM, respectively. We also thank William Bassett for his help with cyclic twinning and mineralogy. L.F.K. is pleased to acknowledge helpful discussions with Peter Ercius. This work was supported in part by Award No. KUS-C1-018-02, made by King Abdullah University of Science and Technology (KAUST). We also acknowledge support of Cornell Center for Materials Research (CCMR) with funding from the Materials Research Science and Engineering Center program of the National Science Foundation (cooperative agreement DMR 0520404), and support of Energy Materials Center at Cornell (EMC^2), an Energy Frontier Research Center funded by the U.S. Department of Energy, Office of Science, Office of Basic Energy Science under Award Number DE-SC0001086.

Supporting Information Available. Materials, synthetic procedures, and characterization for precursors **I**−**VI** and nanocrystals **1**−**9**, electron tomography, purification of TOPO, SAED information, histograms showing the number of arms per nanocrystal for products **1**, **2**, and **3**, Co_2P crystal structure, additional TEM and electron tomography reconstruction images, additional XRD spectra, electron tomography reconstruction movies, and movie captions. This material is available free of charge via the Internet at http://pubs.acs.org.

REFERENCES AND NOTES

(1) Qian, C.; Kim, F.; Ma, L.; Tsui, F.; Yang, P. D.; Liu, J. *J. Am. Chem. Soc.* **2004**, *126*, 1195–1198.
(2) Stein, B. F.; Walmsley, R. H. *Phys. Rev.* **1966**, *148*, 933–939.
(3) Gregg, K. A.; Perera, S. C.; Lawes, G.; Shinozaki, S.; Brock, S. L. *Chem. Mater.* **2006**, *18*, 879–886.
(4) Li, Y.; Malik, M. A.; O'Brien, P. *J. Am. Chem. Soc.* **2005**, *127*, 16020–16021.
(5) Kelly, A. T.; Rusakova, I.; Ould-Ely, T.; Hofmann, C.; Luttge, A.; Whitmire, K. H. *Nano Lett.* **2007**, *7*, 2920–2925.
(6) Brock, S. L.; Perera, S. C.; Stamm, K. L. *Chem.—Eur. J.* **2004**, *10*, 3364–3371.
(7) Lucas, I.; Perez, L.; Aroca, C.; Sanchez, P.; Lopez, E.; Sanchez, M. C. *J. Magn. Magn. Mater.* **2005**, *290*, 1513–1516.
(8) da Silva, R. C.; dos Santos, E. M.; Sartorelli, M. L.; Sinnecker, J. P.; Gundel, A.; Sommer, R. L.; Pasa, A. A. *J. Magn. Magn. Mater.* **2004**, *272*, 1460–1462.
(9) Ni, Y. H.; Li, J.; Jin, L.; Xia, J.; Hong, J. M.; Liao, K. M. *New J. Chem.* **2009**, *33*, 2055–2059.
(10) Ni, Y.; Li, J.; Zhang, L.; Yang, S.; Wei, X. *Mater. Res. Bull.* **2009**, *44*, 1166–1172.
(11) Burns, A. W.; Layman, K. A.; Bale, D. H.; Bussell, M. E. *Appl. Catal., A* **2008**, *343*, 68–76.
(12) Souza, D. C. S.; Pralong, V.; Jacobson, A. J.; Nazar, L. F. *Science* **2002**, *296*, 2012–2015.
(13) Hulliger, F. Crystal chemistry of the chalcogenides and pnictides of the transition elements. In *Structure and Bonding*; Springer: Berlin and Heidelberg, 1968; Vol. 4, pp 83—229.
(14) Schlesinger, M. E. *Chem. Rev.* **2002**, *102*, 4267–4301.
(15) Lukehart, C. M.; Milne, S. B.; Stock, S. R. *Chem. Mater.* **1998**, *10*, 903–908.
(16) Qian, X. F.; Xie, Y.; Qian, Y. T.; Zhang, X. M.; Wang, W. Z.; Yang, L. *Mater. Sci. Eng., B* **1997**, *49*, 135–137.
(17) Micic, O. I.; Curtis, C. J.; Jones, K. M.; Sprague, J. R.; Nozik, A. J. *J. Phys. Chem.* **1994**, *98*, 4966–4969.
(18) Micic, O. I.; Sprague, J. R.; Curtis, C. J.; Jones, K. M.; Machol, J. L.; Nozik, A. J.; Giessen, H.; Fluegel, B.; Mohs, G.; Peyghambarian, N. *J. Phys. Chem.* **1995**, *99*, 7754–7759.
(19) Battaglia, D.; Peng, X. G. *Nano Lett.* **2002**, *2*, 1027–1030.
(20) Lucey, D. W.; MacRae, D. J.; Furis, M.; Sahoo, Y.; Cartwright, A. N.; Prasad, P. N. *Chem. Mater.* **2005**, *17*, 3754–3762.
(21) Xu, S.; Kumar, S.; Nann, T. *J. Am. Chem. Soc.* **2006**, *128*, 1054–1055.
(22) Xie, Y.; Su, H. L.; Qian, X. F.; Liu, X. M.; Qian, Y. T. *J. Solid State Chem.* **2000**, *149*, 88–91.
(23) Hou, H. W.; Yang, Q.; Tan, C. R.; Ji, G. B.; Gu, B. X.; Xie, Y. *Chem. Lett.* **2004**, *33*, 1272–1273.
(24) Hou, H. W.; Peng, Q.; Zhang, S. Y.; Guo, Q. X.; Xie, Y. *Eur. J. Inorg. Chem.* **2005**, 2625–2630.
(25) Park, J.; Koo, B.; Yoon, K. Y.; Hwang, Y.; Kang, M.; Park, J. G.; Hyeon, T. *J. Am. Chem. Soc.* **2005**, *127*, 8433–8440.
(26) Wang, J. L.; Yang, Q.; Zhang, Z. D.; Sun, S. H. *Chem.—Eur. J.* **2010**, *16*, 7916–7924.
(27) Maneeprakorn, W.; Malik, M. A.; O'Brien, P. *J. Mater. Chem.* **2010**, *20*, 2329–2335.
(28) Manna, L.; Scher, E. C.; Alivisatos, A. P. *J. Am. Chem. Soc.* **2000**, *122*, 12700–12706.
(29) Peng, X. G.; Manna, L.; Yang, W. D.; Wickham, J.; Scher, E.; Kadavanich, A.; Alivisatos, A. P. *Nature* **2000**, *404*, 59–61.
(30) Manna, L.; Milliron, D. J.; Meisel, A.; Scher, E. C.; Alivisatos, A. P. *Nat. Mater.* **2003**, *2*, 382–385.
(31) Kanaras, A. G.; Sonnichsen, C.; Liu, H. T.; Alivisatos, A. P. *Nano Lett.* **2005**, *5*, 2164–2167.
(32) Tang, J.; Alivisatos, A. P. *Nano Lett.* **2006**, *6*, 2701–2706.
(33) Xia, Y.; Yang, P.; Sun, Y.; Wu, Y.; Mayers, B.; Gates, B.; Yin, Y.; Kim, F.; Yan, H. *Adv. Mater.* **2003**, *15*, 353–389.
(34) Garcia-Ruiz, J. M.; Melero-Garcia, E.; Hyde, S. T. *Science* **2009**, *323*, 362–365.
(35) Lee, S. M.; Cho, S. N.; Cheon, J. *Adv. Mater.* **2003**, *15*, 441–444.

DOI: 10.1021/nl103400a | *Nano Lett.* **2011,** *11,* 188–197

(36) Corbridge, D. E. C. *Phosphorus—an Outline of Its Chemistry, Biochemistry and Technology*, 5th ed.; Elsevier: Amsterdam, 1995; p 1208.
(37) Chen, J. H.; Tai, M. F.; Chi, K. M. *J. Mater. Chem.* **2004**, *14*, 296–298.
(38) Khanna, P. K.; Jun, K. W.; Hong, K. B.; Baeg, J. O.; Mehrotra, G. K. *Mater. Chem. Phys.* **2005**, *92*, 54–58.
(39) Henkes, A. E.; Schaak, R. E. *Chem. Mater.* **2007**, *19*, 4234–4242.
(40) Henkes, A. E.; Vasquez, Y.; Schaak, R. E. *J. Am. Chem. Soc.* **2007**, *129*, 1896–1897.
(41) Dockner, T. Reduction of teritiary phosphine oxides, phosphine sulfides or phosphine dihalides with hydrocarbons. US Patent 4727193, 1988.
(42) Barea, E.; Batlle, X.; Bourges, P.; Corma, A.; Fornes, V.; Labarta, A.; Puntes, V. F. *J. Am. Chem. Soc.* **2005**, *127*, 18026–18030.
(43) Sekine, T.; Osada, K.; Hokura, A. *Bull. Chem. Soc. Jpn.* **1996**, *69*, 1565–1571.
(44) The shape and size of NPs in Figure 5 show some differences compared to those of Figure 1a. This is likely due to the partial dissolution/decomposition of the end part of NPs after a long period (>2 months) in solution .
(45) Fujii, S.; Ishida, S.; Asano, S. *J. Phys. F: Met. Phys.* **1988**, *18*, 971–980.
(46) Jun, Y. W.; Choi, J. S.; Cheon, J. *Angew. Chem., Int. Ed.* **2006**, *45*, 3414–3439.
(47) He, J. H.; Han, M.; Shen, X. P.; Xu, Z. *J. Cryst. Growth* **2008**, *310*, 4581–4586.
(48) Granasy, L.; Pusztai, T.; Tegze, G.; Warren, J. A.; Douglas, J. F. *Phys. Rev. E* **2005**, *72*, No. 0116051—01160515.
(49) Magill, J. H. *J. Mater. Sci.* **2001**, *36*, 3143–3164.
(50) Granasy, L.; Pusztai, T.; Borzsonyi, T.; Warren, J. A.; Douglas, J. F. *Nat. Mater.* **2004**, *3*, 645–650.
(51) Pusztai, T.; Bortel, G.; Gránásy, L. *Mater. Sci. Eng., A* **2005**, *413—414*, 412–417.
(52) Lehman, L. P.; Xing, Y.; Bieler, T. R.; Cotts, E. J. *Acta Mater.* **2010**, *58*, 3546–3556.
(53) Picture courtesy of Joan Rosell, Grup Mineralògic Català, Barcelona.
(54) Lim, B.; Wang, J.; Camargo, P. H. C.; Cobley, C. M.; Kim, M. J.; Xia, Y. *Angew. Chem., Int. Ed.* **2009**, *48*, 6304–6308.
(55) Xia, Y.; Xiong, Y.; Lim, B.; Skrabalak, S. E. *Angew. Chem., Int. Ed.* **2009**, *48*, 60–103.
(56) Wang, Z. L. *J. Phys. Chem. B* **2000**, *104*, 1153–1175.
(57) Carbone, L.; Kudera, S.; Carlino, E.; Parak, W. J.; Giannini, C.; Cingolani, R.; Manna, L. *J. Am. Chem. Soc.* **2006**, *128*, 748–755.

DOI: 10.1021/nl103400a | *Nano Lett.* **2011,** *11,* 188–197